On Modeling Bonds in Fused, Porous Networks: 3D Simulations of Fibrous–Particulate Joints

L. BERHAN[1] AND A. M. SASTRY[1,2]*
[1]*Department of Mechanical Engineering*
[2]*Department of Biomedical Engineering*
University of Michigan
Ann Arbor, MI 48109-2125, USA

ABSTRACT: The deformation and failure of fused, porous networks are key concerns in microscale power sources and open trusses for structural applications. We have found that the behavior of the connection points in these open networks is the most critical determinant of materials response. For many manufacturable material geometries, both stiffness and strength are largely controlled by these interparticle or interelement bonds, rather than by the response of the longer aspect ratio sections. Classic work in sintered materials is of limited applicability in this context, since formation of multiphase porous networks often involves volume-conserving interconnects, or fused sections created by additional material, rather than via (heated) compaction of particles or elements. Here we expand on previous work in 2D network behavior (reviewed in [1]) by focusing on the geometry and response of 3D interconnects between cylindrical elements. We present computational results for deformation of 3D interconnects in a large class of stochastic fibrous and particulate structures. Further, we suggest methodologies for adapting tractable 2D simulations to account for the known 3D stress-enhancing effects. We conclude with some comments on limiting strengths and toughnesses in these materials, and suggest divisions for classifications of these porous network bonds.

KEY WORDS: bonds, deformation, fiber, fused, joint, mechanics, nanotube, network, random, sintered, welded.

INTRODUCTION

EXAMPLES OF FUSED networks of fibers and/or particles can be found both in natural and in manufactured porous materials. These include the electrodes used in NiMH

*Author to whom correspondence should be addressed. E-mail: amsastry@engin.umich.edu

0021-9983/03/08 0715–26 $10.00/0 DOI: 10.1177/002199803029725

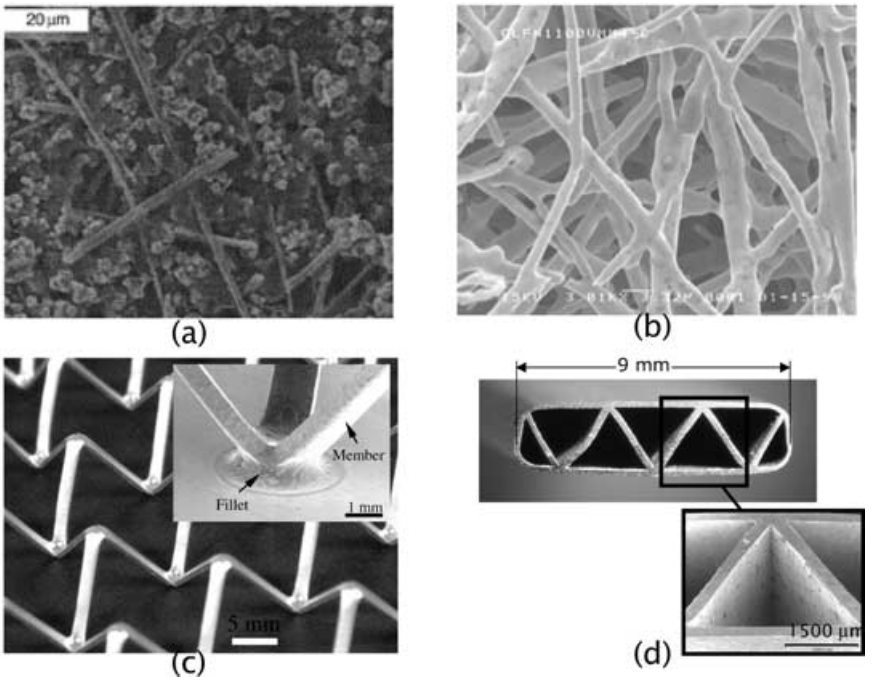

Figure 1. *Examples of real fused materials. (a) Scanning electron micrograph of $LiCoO_2$ cathode with 7 wt.% fiber. (Image reproduced from [39] by permission of The Electrochemical Society, Inc.); (b) SEM image of sintered nickel fibers of a filter assembly (Photo courtesy Pall Corporation, East Hills, New York.); with inset of the core–facesheet bond. (Image adapted from [40] with permission.); (d) Triangular core panel of an alloy honeycomb structure manufactured using cell extrusion (Photo courtesy Professor Joe Cochran, School of Materials Science and Engineering, Georgia Institute of Technology, Atlanta, Georgia).*

(nickel-metal hydride) and Li-ion (lithium ion) batteries that contain porous metallic or carbon substrates (Figure 1(a)), gas filters comprised of sintered metal fibers (Figure 1(b)), and space trusses manufactured of cast or extruded metals (Figure 1(c) and (d)); porous nanotube mat are among the newest engineered materials constructed in this way. Applications for this general class of materials are numerous, and span many size scales.

Introduction of multiple functionalities in these porous materials often necessitates use of multiple phases, resulting in composite materials wherein one or more phases may have purely structural functions, and one or more may have, for example, electrochemical, actuation or sensing functions. Analysis of the underlying structure is a critical first step in creating composites which satisfy all such design criteria, so here we focus only on structural properties. We also note that these models are designed to be part of a strategy in simplifying analysis of composite structures. Here, we perform detailed analyses of the material joints, since we have found these to be of critical importance in nontriangulated (statically indeterminate) porous structures; Figure 2 illustrates the strategy.

The network generation approach used here was previously described by Sastry et al. [2]. Briefly, fibers are placed randomly (by centerpoint) within a unit cell for analysis; after application of periodic boundary conditions to the cell and removal of unbonded ends in the array, the cell is loaded electrostatically or mechanically. This general methodology

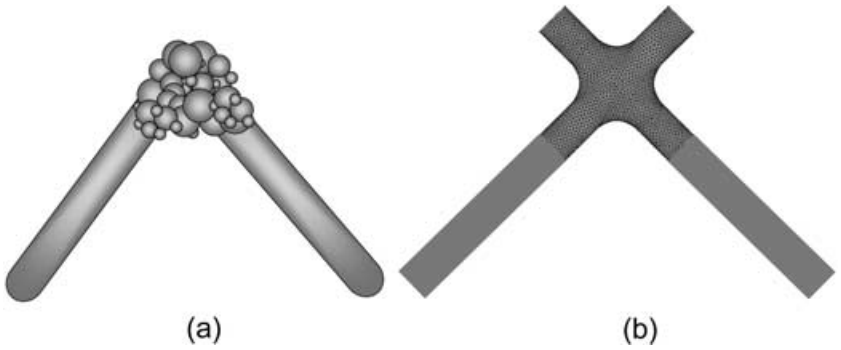

Figure 2. *Strategies for analysis of a composite joint (adapted from [1]), e.g. (a) two ''beam'' members joined by a porous bond, as with carbon fibers in a Li-ion battery joined by binder material (adapted from); (b) possible representation of the joint properties via a ''compliant zone'' near the joint with distinct properties.*

for studying stochastic networks has been used to investigate electrical conduction properties [3,4] and mechanical deformation and failure [5–8] of porous battery substrates. Since the stochastic approach allows study of networks arising from a statistical distribution of geometric variables, we have also studied the effect of mild alignment in networks [4] as would arise from shear flow induced manufacturing processes (e.g. papermaking). Earlier, numerical network models of porous, fibrous materials had been used to obtain bounds on the mechanical properties (for example [9–11]) and in the prediction of transport properties [12].

We are particularly interested in improved design of NiMH and Li-ion battery materials [13,14]. The performance of porous battery materials is greatly influenced by the nature of the particle interconnects [8]. We initially modeled these interconnects as rigid bonds or torsion spring-bonded joints [6,8]. Later, we showed that the use of a torsion spring joint model was equivalent to assumption of a ''compliant zone'' at the interconnect, allowing analysis of networks in which struts or particles are connected with a lower modulus (e.g. porous particulate or adhesive) second phase [6]. These two-dimensional (2D) simulations showed that network behavior is relatively insensitive to detail in modeling the response of constituent ''struts,'' or long cylindrical beams in these networks (i.e. Timoshenko vs. Euler beam assumptions result in similar predictions for network response, per [8]).

It is impractical at the present time to explicitly model the microarchitectured materials of interest via fully three-dimensional (3D) finite element analysis. Our overall strategy is to inform more tractable 2D network analysis parameters obtained for a broad range of joint morphologies, using 3D analyses. Our main objectives in this paper were thus threefold:

1. Develop a methodology for specifying bond architecture in fused cylindrical networks, which spans a large, practical range of engineered structures,
2. Determine, through 3D finite element analysis, the locations and probable magnitudes of local loads arising in bonded cylinders of various orientation and interpenetration, and
3. Develop a simple model for the behavior of these joints, to refine more efficient 2D network simulations.

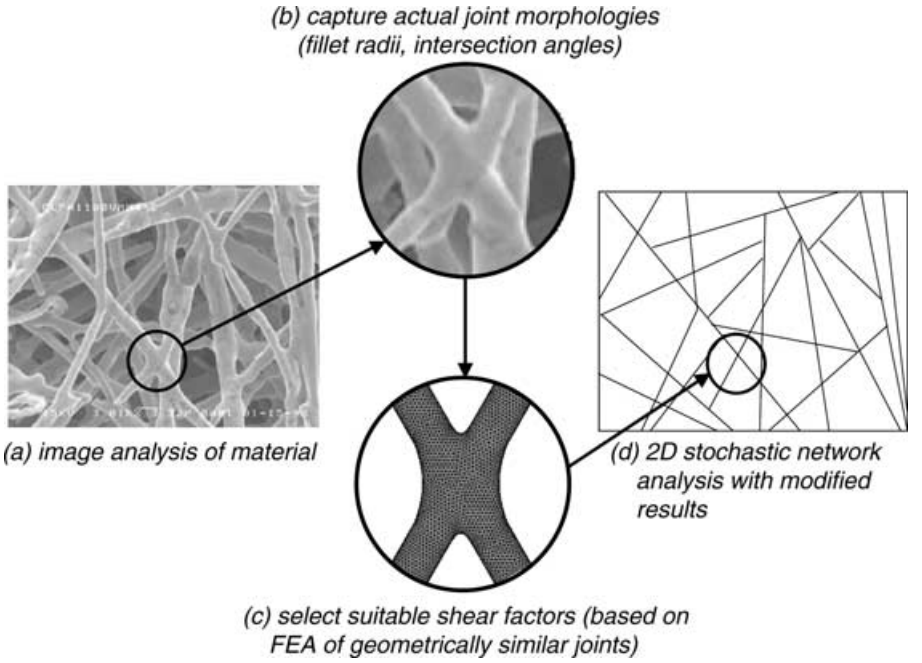

Figure 3. *Schematic of steps involved in implementing 3D modification methods in 2D stochastic network analysis.*

The general methodology is outlined in Figure 3. The likely range of morphologies present is first determined by detailed image analysis. Then, 3D finite element analyses are preformed for all relevant joint morphologies, creating a database of specific joint responses. Simplified models are developed to empirically relate the maximum stress in each joint to its geometry. This in turn can be readily implemented as a local strain- or stress-based failure criterion in a 2D network simulation [e.g. 8].

PREVIOUS WORK AND MODELING OVERVIEW

Modeling Joint Architectures in Joined Structural Members

The materials of interest span a wide range of joined, porous materials, including sinter-bonded mats and truss structures. Previous models for sintered joints generally have been focused on representation of the axisymmetric joints between spherical particles. Our materials' joints are not axisymmetric, however, and join cylindrical, rather than spherical particles.

Nonetheless, previous geometric assumptions in bonded materials provide some insight into the modeling of "fillets" or connecting material, for the present cases. For example, Kuczynski [15] presented an early solution for the geometry of a sphere sintered to a flat plane, producing a circular interface with 'necks' of circular profile tangent to both sphere and the plane. This basic geometry has formed the basis for many sintering models [16]. Angled flexural members have also been studied previously by finite element analysis

using a fillet-type joint, and it has been shown for rectangular-section solid, angled members, that increasing the corner fillet radius results in a decrease in stress concentration (e.g. [17]).

The joints of interest here do not readily fall into any of the classifications commonly described [e.g. 18], since they are generally "imperfect" in the sense that the two cylindrical parts joined do not completely intersect one another. Thus, we define a new parameter, the degree-of-intersect (d.o.i.), as

$$\text{d.o.i.} = \frac{d}{T}, \tag{1}$$

where d is the diameter of the cylinders, and T is the width of the joint, as shown in Figure 4. A positive, finite value of d.o.i. results for all possible interpenetrations, with bounding values for cases where the fibers are tangential to one another (d.o.i. = 0.5, or have intersecting axes (d.o.i. = 1.0).

In our model we use fillets of circular profile, and further assume that volume of the cylinder material is conserved. Figure 5 is an example of the joint model used in our analyses.

Modeling Stress Enhancement in Joined Structural Members

Stress concentrations necessarily arise at an intersection of two cylindrical members, e.g. tubular joints of offshore platforms, nozzles in pressure vessels, and pipelines, as a result of the geometric discontinuity between intersecting surfaces. Stress concentrations arising in bonded, hollow cross-section members have been published in standard references (e.g. [19,20]). However, neither solutions obtained via the theoretical shell

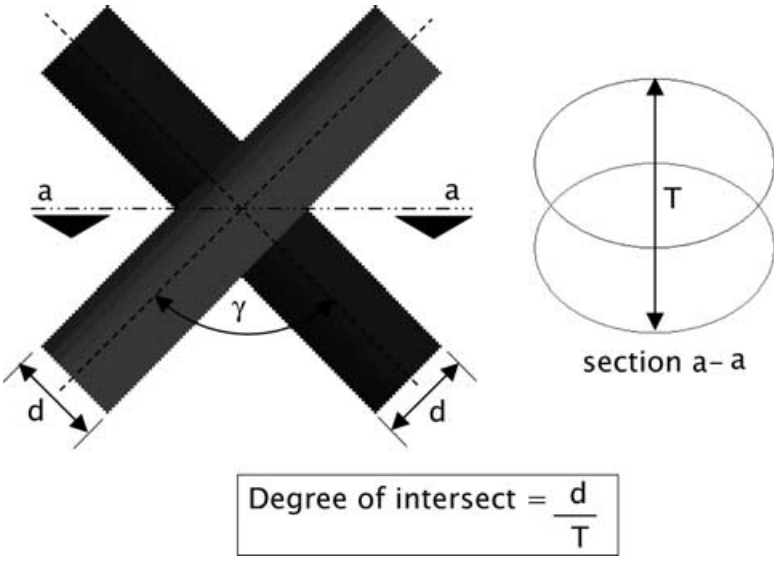

Figure 4. *Definition of the degree-of-intersect (d.o.i.).*

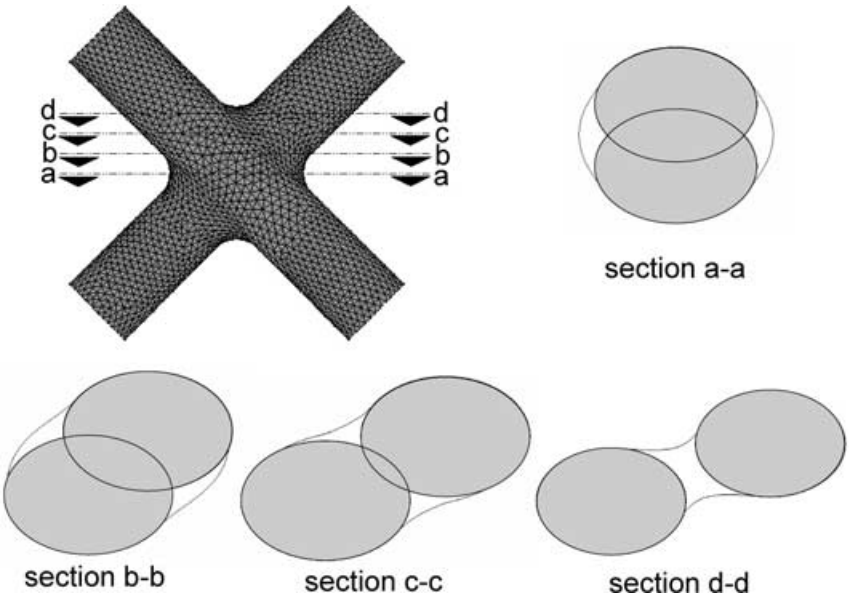

Figure 5. *Sections through two cylinders intersecting at $\gamma = 90^\circ$ and d.o.i. $= 0.65$ with fillet included (fillet and cylinders shown in white and grey respectively in section views). Sections with and without the fillet show that the sharp corners (and hence the stress singularities) are eliminated through the introduction of the fillet.*

theory approach (e.g. [21–24]) nor experimentally derived, geometry-specific stress concentration factors (e.g. [25,26]) are applicable to the general problem of imperfectly bonded cylinders of solid cross-section.

Here, we develop a model for two intersecting beams of circular cross section using solid elements. Stress singularities produced by sharp corners can be handled by introduction of smooth fillets to eliminate geometric singularities, or by use of specially formulated elements (e.g. quarter-point elements, per [27,28]). Finite element analysis of intersecting cylindrical shells often involves the use of specially formulated elements [e.g. 18,29]. These analyses can be used to predict crack growth at the intersection of the members, and generally do not include smoothing fillets. However, published images of both man-made sintered metal networks and naturally occurring biological networks show that the intersection of any two fibers produces a fillet of finite radius at the point of contact (for example Figure 1(b)). Thus, the inclusion of a fillet at the joint in the finite element analysis not only addresses the numerical problem, but also more accurately represents the actual material, and the use of special elements to handle stress singularities is not required.

In this paper we use a shear factor to describe the effect of varying d.o.i, based on simulations of joints of a range of geometries. We chose the use of a shear factor over a stress concentration factor because calculation of the latter would require a choice of location to measure nominal stress.

The concept of using shear factors to develop expressions for the response of beams, particularly those of complex or nonhomogeneous geometries, has been widely used. In

analysis of linear elastic, isotropic, thick beams, for example, transverse shear effects are significant and use of the Timoshenko beam theory is recommended; a shear correction factor has been used to account for the variation in shear stress through the cross-section of the beam. This shear factor depends on the beam geometry, material, loading, and boundary conditions [30]. Commonly used shear factors for various cross-sectional geometries have been tabulated in some texts (e.g. [31,32]), and the topic is the subject of continued research (e.g. [33,34]).

The increased use of composites in the 1970s and 1980s [35] generated much interest in the analysis of laminated beams. For laminated beams and plates in bending, coupling of shear and bending occurs, and shear deformation is significant, and has been analyzed via a layerwise application of the Timoshenko beam theory [30,36]. For static analyses, the required shear factors have been determined from linear elastic theory [e.g., 37,38].

Here, we develop a shear factor to relate the maximum stress in the 3D simulations to maximum stresses in the 2D cases. In this way, we provide a simple technique for estimating the stress enhancement in complex joints. We first describe our geometric model and compare stresses in our 3D finite element simulations with 2D results generated by our previous approaches for multibeam assemblies. Then we characterize the relationship between the stresses via the fitted shear factor.

A THREE-DIMENSIONAL MODEL FOR GEOMETRY OF INTERCONNECTS BETWEEN CYLINDRICAL MEMBERS

For any pair of cylinders intersecting with angle, γ, and d.o.i., we assume that the projection of a section cut through the joint along the axis of either cylinder, is a circular arc of radius R, tangent to both cylinders, as shown in Figure 6(a). These tangent lines are labeled 1–4 in Figure 6(b). The lines connecting the end points of these lines lie on the surfaces of the cylinders (lines 5–12 of Figure 6(b)), and form circular arcs of radius R' when projected onto a plane through the axis of that cylinder as shown in Figure 6(a).

We define aspect ratio as

$$\text{aspect ratio} = \frac{L}{d}, \tag{2}$$

where L is the sum of the lengths of the two beams in the assembly.

The twelve lines created are then splined to form four surfaces. The lines defining each surface are shown in Figure 6(c) and (d). Figure 7(a) shows HyperMesh® meshes of surfaces (labeled Surfaces 1–4). The original cylindrical surfaces are trimmed with lines 5–8 and 9–12 respectively, and the portions of the original surfaces enclosed by these lines are removed. The remaining surfaces are meshed in Figure 7(b). The ends of the cylinders are splined and meshed (Figure 7(c)). These combined surfaces enclose a single continuous volume. 2D meshes of these surfaces are shown in Figure 7(d); they are used to create a mesh of 3D elements to fill the volume. For each simulation, the volume of the 3D elements was calculated in HyperMesh® and this volume compared to that required for volume conservation. The modeling process was repeated with different values of R so as to choose the fillet radius that conserved volume. Several examples of joints analyzed are shown in Figures 8 and 9.

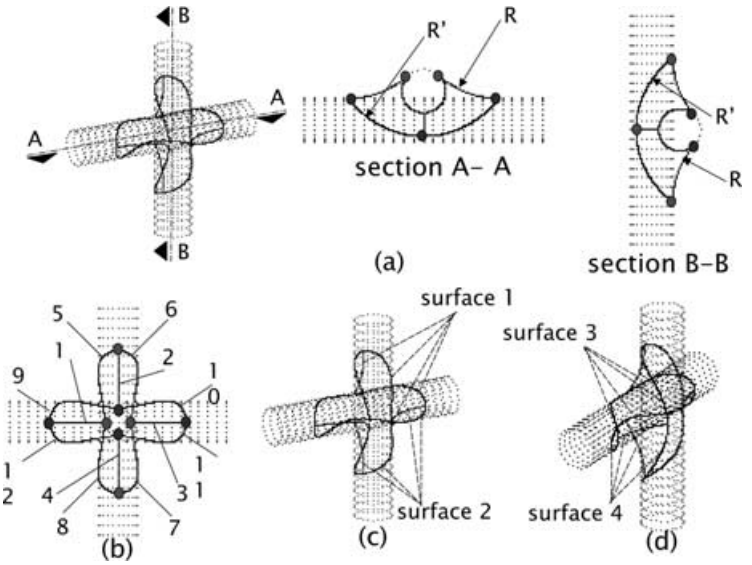

Figure 6. *Steps involved in the creation of the volume-preserving fillet: (a) Cross-sections through a typical*

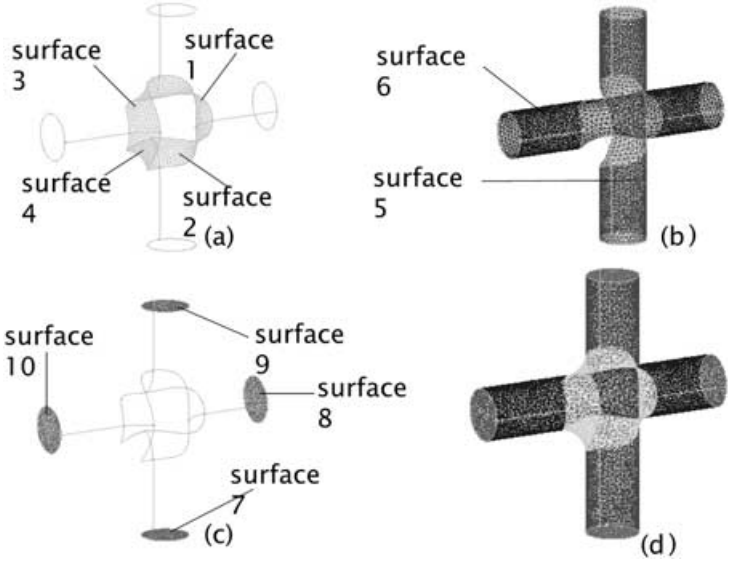

Figure 7. *Generation of the 2D mesh from which the 3D finite element mesh for the volume-preserving joint is created.*

Two-dimensional elements on surfaces 7 and 8 (Figure 7(c)) were dragged distances of $L_1 - 2.5d$ and $L_2 - 2.5d$ respectively, and 3D elements were created along this length. The entire model was then rotated so that the final orientation was as shown in Figure 10. For all the models created, the joint region was modeled to include a portion of each cylinder that measured five times the cylinder diameter.

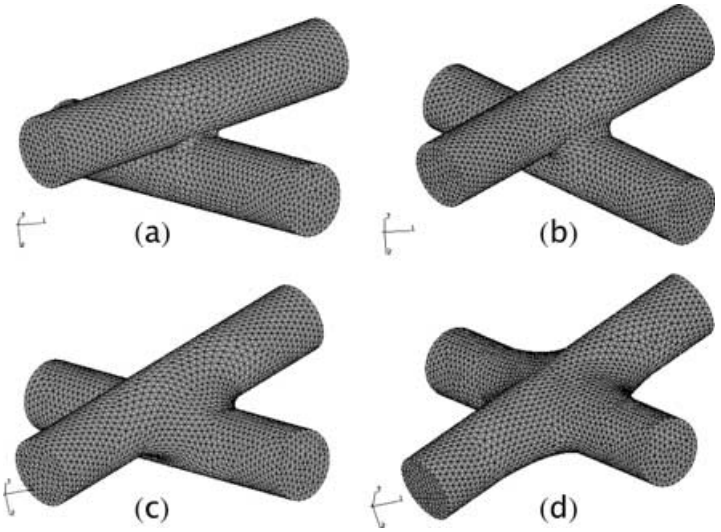

Figure 8. *Finite element model of joint with $\gamma = 90^\circ$ and (a) d.o.i. = 0.52; (b) d.o.i. = 0.55; (c) d.o.i. = 0.65; and (d) d.o.i. = 0.85.*

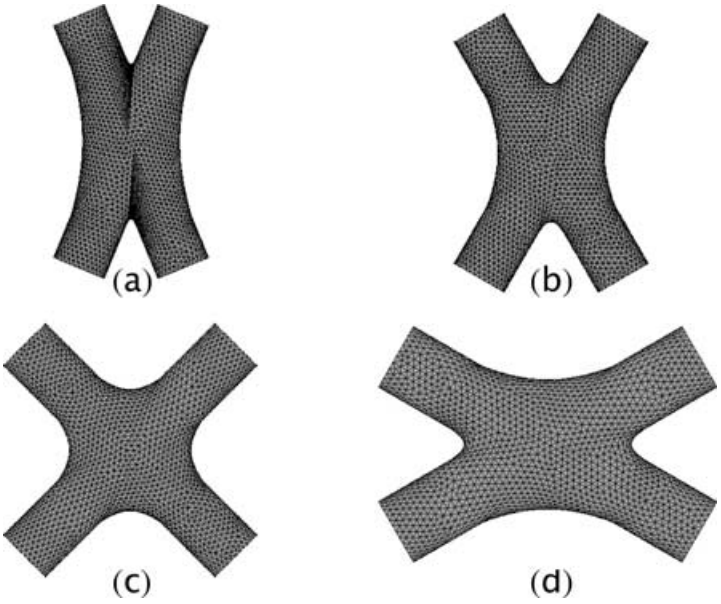

Figure 9. *Finite element model of joint with d.o.i. = 0.85 and (a) $\gamma = 45^\circ$; (b) $\gamma = 60^\circ$; (c) $\gamma = 90^\circ$; and (d) $\gamma = 120^\circ$.*

An aspect ratio of 100 was used for all of our analyses, with relative lengths chosen such that $1 \leq L_1/L_2 \leq 10$. Thus, even for the limiting case of $L_1/L_2 = 10$, the shorter beam segment has an aspect ratio $L_2/d = 9.09$, reasonably allowing use of Euler beam theory for the full range of values of L_1/L_2. This range also enables us to conveniently plot results on a log scale such that $0 \leq \log(L_1/L_2) \leq 1$.

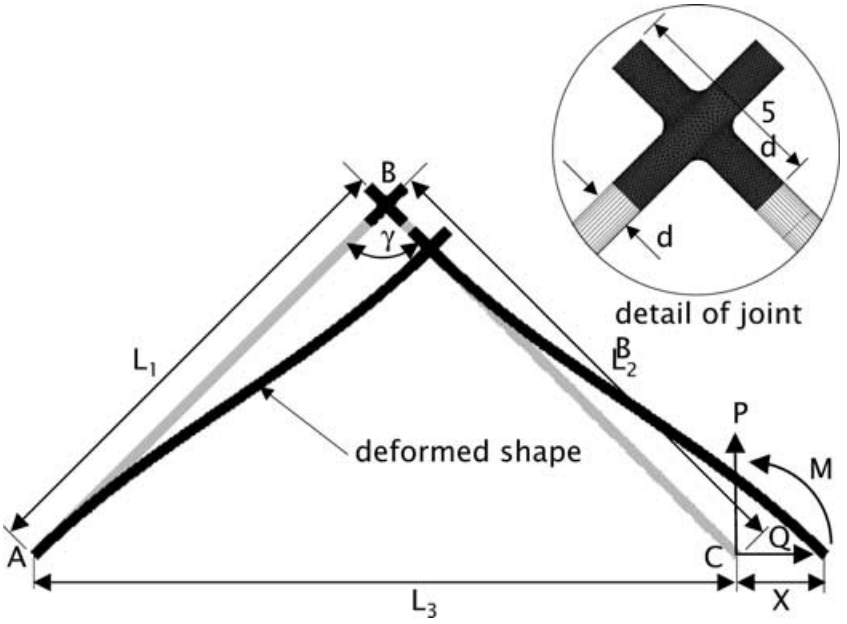

Figure 10. *Example of the finite element model used, with a detail of the joint region.*

3D FINITE ELEMENT ANALYSIS OF THE DEFORMATION OF JOINED MEMBERS

3D Finite Element Simulations of Joint Deformation

For each model shown in Figure 10, end A was fixed and all nodes on end C were displaced (X). These displacements were always taken as unity, i.e. $X = d$. The sum of the nodal reaction forces in the x-direction at end C, Q, was determined, along with the magnitude and location of the maximum von Mises stress in the joint region. The results for "structural modulus" were obtained, per

$$E_{\text{effective}} = \frac{QL_3}{AX}, \tag{3}$$

where X is the applied displacement in the x-direction at end C, A is the cross-sectional area of the members, and Q is the total reaction force at C in the x-direction. To verify our implementation, effective moduli were compared with those obtained for deformation of an equivalent 2D assembly (Figure 10), rigidly connected at B. M, P, and Q are the resulting moment, vertical and horizontal forces at end C when that end is given a displacement X in the x-direction. As required for equilibrium, the results for $E_{\text{effective}}$ obtained were essentially identical for 2D and 3D analyses, regardless of d.o.i.

Figure 11 shows the stress distribution obtained at the joint for $\gamma = 90^\circ$, $L_1 = L_2$, and four different d.o.i. For all the angles and d.o.i. considered, the maximum stress at the joint was found to be higher than the value predicted by the equivalent 2D models, with

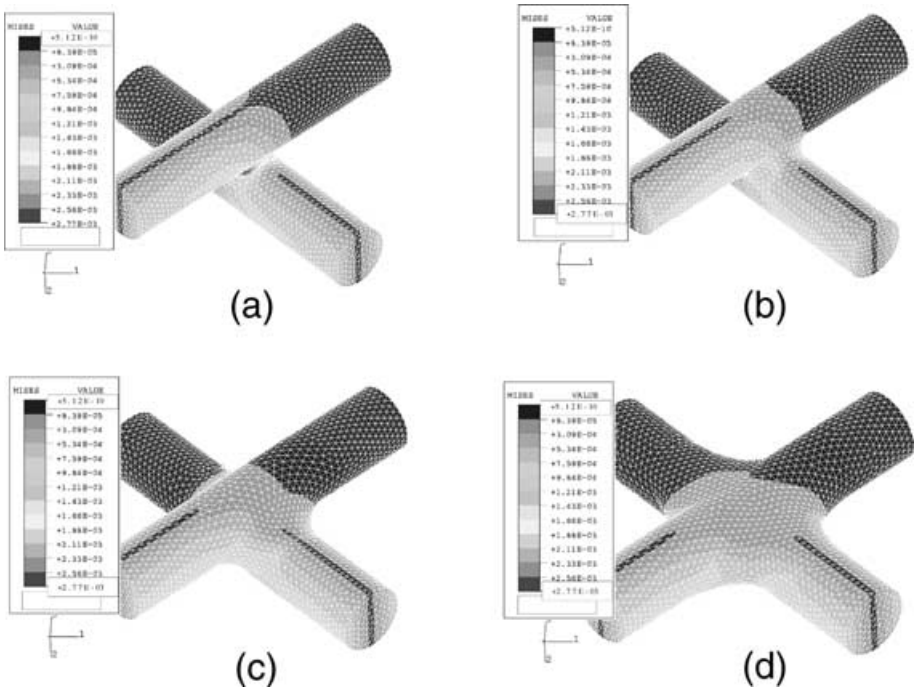

Figure 11. *von Mises Stress contours (normalized with E) at joint for $\gamma = 90^\circ$, $\varepsilon = 0.014$, $L_1/L_2 = 1$ and (a) d.o.i. = 0.52; (b) d.o.i. = 0.55; (c) d.o.i. = 0.65; and (d) d.o.i. = 0.85.*

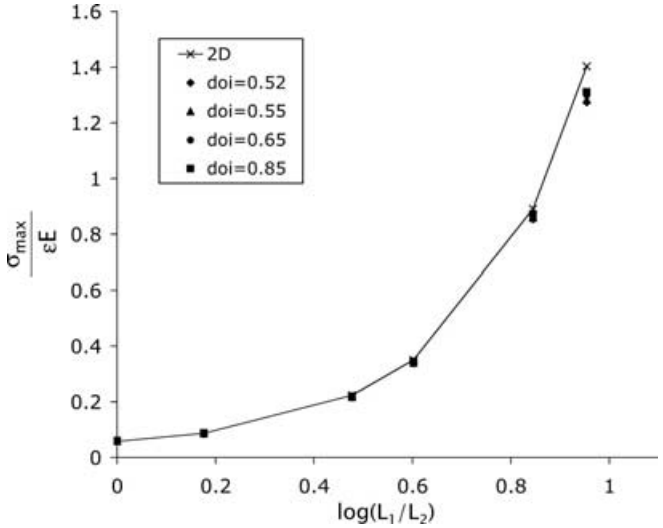

Figure 12. *Maximum normalized stress at a distance L_e from end C for $\gamma = 90^\circ$.*

the maximum joint stresses inversely related to d.o.i. For example, for intersection angle $\gamma = 90^\circ$ and $L_1/L_2 = 1$, the ratios of maximum joint stress in the 3D versus 2D simulations were 3.2, 1.7, and 1.3 for d.o.i. values 0.52, 0.55, and 0.65 respectively. Also, for $\gamma \leq 90^\circ$, maximum 3D joint stresses increased, relative to their 2D counterparts, with decreasing

intersection angle, for all combinations of d.o.i. and length ratio examined. For example, for d.o.i. $= 0.65$ and $L_1/L_2 = 1$, the maximum joint stresses in the 3D simulations were found to be 3.9, 2.3, and 1.7 times the joint stress of the corresponding 2D simulations for intersection angles of 45, 60 and 90°, respectively.

A Shear Factor Approach for Interpretation and Application of Finite Element Simulations

In order to model the maximum local stress in the 3D joint by performing the simple 2D analysis, we use a shear factor, S to modify results for maximum stresses. In a 2D model, shear stresses at the joint are assumed to be negligible (Euler beam assumption), and thus the maximum stress at joint B is given by the greater of

$$\sigma_{2D} = \frac{F_{AB}}{A} \pm \frac{M_B r}{I}, \quad \text{or}$$
$$\sigma_{2D} = \frac{F_{BC}}{A} \pm \frac{M_B r}{I} \tag{4}$$

where F_{AB} and F_{BC} are the axial forces in members AB and BC, M_B is the bending moment at B, r is the radius and I is the second moment of area of each member. For comparison with the 2D analyses, we determined the resulting 3D stresses in the form of a von Mises stress, following the familiar expression

$$\sigma_{vm} = \frac{1}{\sqrt{2}} \sqrt{(\sigma_x - \sigma_y)^2 + (\sigma_x - \sigma_y)^2 + (\sigma_x - \sigma_y)^2 + 6\left(\tau_{xy}^2 + \tau_{yz}^2 + \tau_{zx}^2\right)}. \tag{5}$$

The maximum (von Mises) stress at a cross section some distance away from the joint for the 3D simulations was found to converge to the 2D solution, as seen in Figure 12. At the joint, however, the stresses were much greater than those in an equivalent 2D model. The large deviation of the maximum von Mises stress at the joint from that of an equivalent 2D model suggests that shear stresses are dominant at the joint for the 3D model. As expected, this effect becomes more pronounced with decreasing d.o.i.

For d.o.i. < 1, where the axes of the members do not intersect, the shear stress at the joint is due to the offset of the axes of the fused members. We assume that this resulting shear stress at the joint is unidirectional (and thus constitutes one component of shear stress), and is proportional to the bending moment at the joint. We further assume that this stress and the normal stresses in each of the members of the assembly are the only stresses present at the joint, and rewrite the von Mises stress (Equation (5)) as

$$\sigma_{vm} = \sqrt{\sigma_x^2 + 3\tau_{xy}^2}, \tag{6}$$

introducing a shear factor, S, such that $\tau_{xy} = SM_B$. The maximum normal stress at the joint in the 3D model is the same as that of the 2D model (σ_{2D} in Equation (4)).

Substituting for σ_x and τ_{xy} in Equation (6), and normalizing all terms in the equation we can express the maximum normalized von Mises stress at the joint in three dimensions as

$$\sigma'_{3D} = \sqrt{\sigma'^2_{2D} + 3\left(S' M'_B\right)^2} \tag{7}$$

where $\sigma'_{3D} = \sigma_{3D} L_3/(EX)$, $\sigma'_{2D} = \sigma_{2D} L_3/(EX)$, $M'_B = M_B L_3/(Xr^3 E)$, and $S' = Sr^3$.

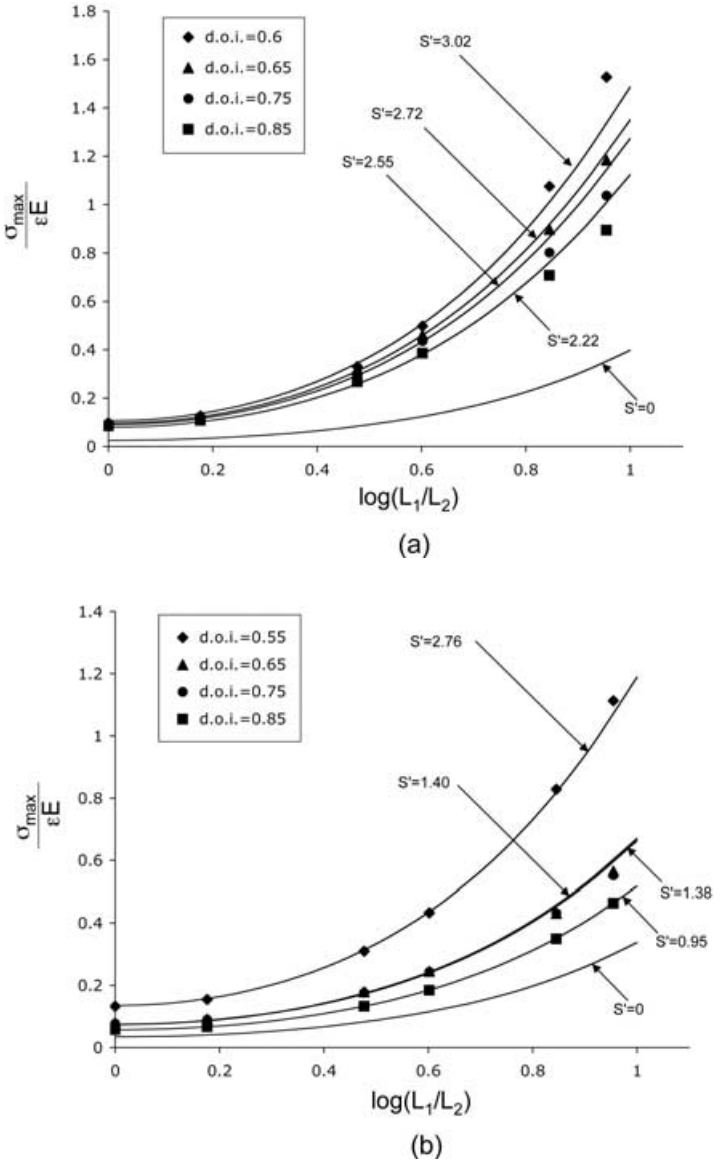

Figure 13. *Maximum normalized stress at joint for: FEA results and 2D results modified with normalized shear factor S′ for (a) $\gamma = 45^\circ$; (b) $\gamma = 60^\circ$; (c) $\gamma = 90^\circ$; (d) $\gamma = 120^\circ$.*

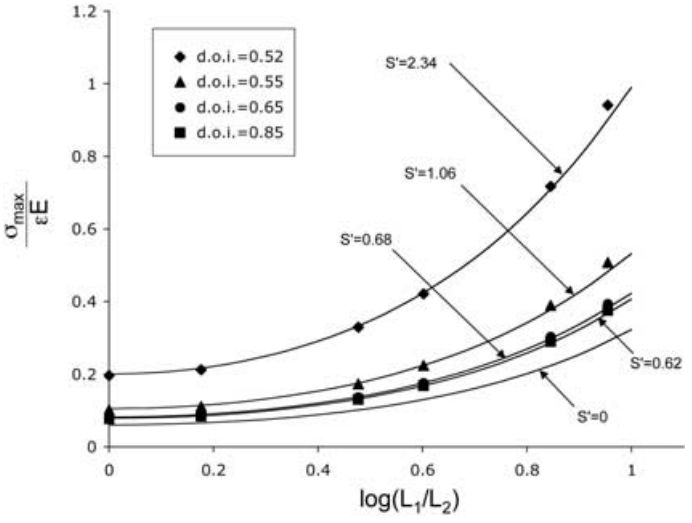

(c)

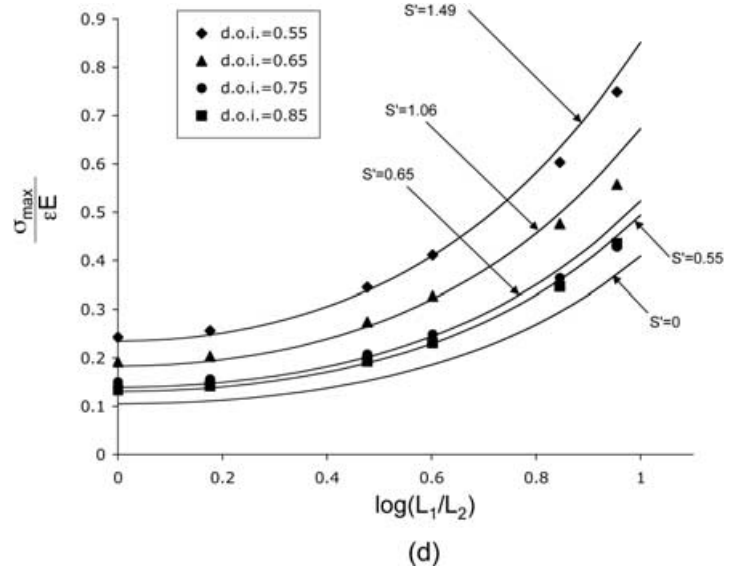

(d)

Figure 13. *Continued.*

For each of our finite element simulations, M_B and the maximum normalized 2D and 3D joint stresses, σ'_{2D} and σ'_{3D}, were substituted into Equation (7). The equation was then solved for S'. For each case of intersection angle and d.o.i., an average of the six unique S' values obtained from the six different length ratios considered was calculated. These averaged values of S' were then substituted in Equation (7), and σ'_{3D} plotted with the 3D finite element results as shown in Figure 13.

Figure 13 shows that the finite element results for the combinations of d.o.i. and γ considered are well fit with the expression for σ'_{3D} of Equation (7), given a suitable choice of shear factor, S'.

A COMPLIANT ZONE MODEL FOR INTERCONNECT PROPERTIES

In prior work [5], we modeled the joint response of 2D networks with torsion springs (e.g. the one shown in Figure 14(a)) in determining mechanical properties of battery substrates. We also [6] proposed use of a compliant zone model to handle cases in which enhanced or reduced local joint stresses arose from use of another material (bonding) phase. In this section, we further investigate use of the model through comparisons of effective modulus of torsion spring and equivalent compliant zone models using finite element analysis.

Validation of the Compliant Zone Model: Finite Element Analysis

In [6] we considered a structure comprised of two multiphase beams similar to the one shown in Figure 15, and compared this to an equivalent torsion spring model (as shown in Figure 14(b)); we previously examined the specific case $L_1 = L_2$. By prescribing a virtual displacement at end C of each assembly and equating the resulting forces in the horizontal, vertical and angular directions at C for both models, we presented a solution for the moduli of the two phases of the given modulus compliant zone model and spring constant of the equivalent torsion spring model.

Here we derive a more general form of the compliant zone model, allowing unequal beam segment lengths AB and BC and a compliant zone of length l_c in each beam segment (Figure 15). The beams have uniform cross-sectional area, A, and compliant zone modulus E_c, with the remainder of the beam having modulus E. The equivalent torsion spring model is shown in Figure 14(b). For both models, end A was fixed.

The potential energy of the torsion spring assembly is given by

$$U = \int_0^{L_1} \frac{F_{AB}^2}{2EA} + \frac{M_{AB}^2}{2EI} d\xi_1 + \int_0^{L_2} \frac{F_{BC}^2}{2EA} + \frac{M_{BC}^2}{2EI} d\xi_2 + \frac{M_{AB}(L_1)^2}{2K}, \tag{8}$$

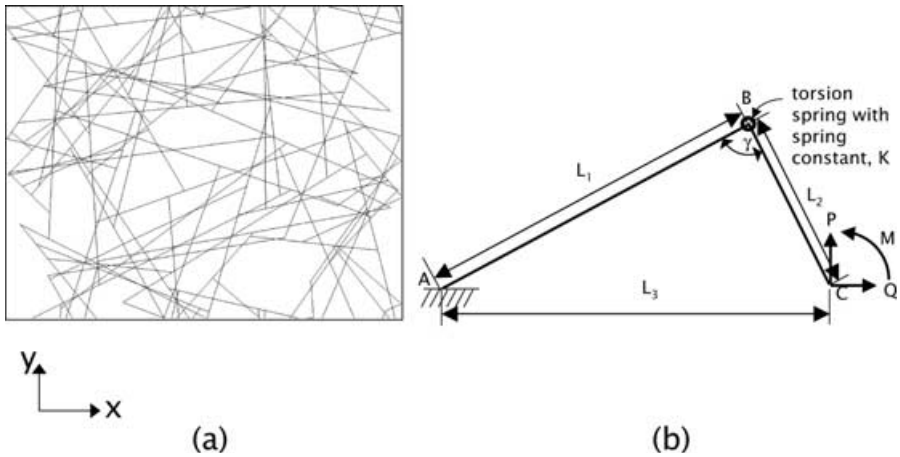

Figure 14. *2D compliant zone model with detail of joint model used for 3D FE analysis of compliant zone model.*

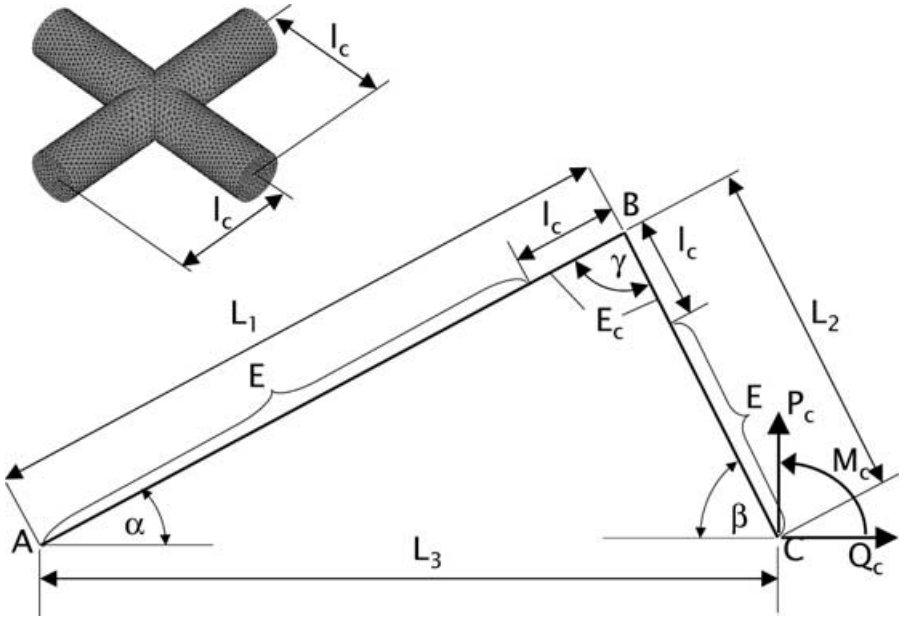

Figure 15. *(a) Reduced 2D random network: 2D network with original volume fraction 29%, reduced for load bearing in y-direction (reduced volume fraction −26%). Torsion springs are used in 2D network analyses as a means of modeling physically imperfect bonds in real materials; (b) Two-beam assembly with torsion spring at joint.*

where ξ_1 is a local coordinate along member AB, with origin at A, and ξ_2 is a local coordinate along BC with origin at C. The potential energy of the compliant zone model may be expressed as

$$U = \int_0^{L_1-\ell_c} \frac{F_{AB}^2}{2EA} + \frac{M_{AB}^2}{2EI}\,d\xi_1 + \int_{L_1-\ell_c}^{L_1} \frac{F_{AB}^2}{2E_cA} + \frac{M_{AB}^2}{2E_cI}\,d\xi_1 + \int_0^{L_2-\ell_c} \frac{F_{BC}^2}{2EA} + \frac{M_{BC}^2}{2EI}\,d\xi_2 + \int_{L_2-\ell_c}^{L_2} \frac{F_{BC}^2}{2E_cA} + \frac{M_{BC}^2}{2E_cI}\,d\xi_2. \tag{9}$$

For both models, we define the horizontal, vertical and angular displacements at C as X, Y, and Θ, respectively. The displacements at end C for the compliant zone model are given by

$$\frac{\partial U}{\partial Q} = X$$
$$\frac{\partial U}{\partial P} = Y \tag{10}$$
$$\frac{\partial U}{\partial M} = \Theta$$

For the torsion spring model, these displacements are

$$\begin{aligned} \frac{\partial U}{\partial Q_c} &= X \\ \frac{\partial U}{\partial P_c} &= Y \\ \frac{\partial U}{\partial M_c} &= \Theta \end{aligned} \tag{11}$$

We set $Y = 0$ and $\Theta = 0$ for both systems, and solve Equations (10) and (11) simultaneously for unknown forces and moments Q, P, M, Q_c, P_c, and M_c. We thus find, for a given assembly, a torsion spring constant for an equivalent torsion spring model such that

$$\begin{aligned} Q &= Q_c \\ P &= P_c \\ M &= M_c \end{aligned} \tag{12}$$

We verified that the model agreed with our finite element implementation, by modeling an assembly containing beams of circular cross-section of diameter d. Based on our analyses using the volume-conserving fillet model, the structural modulus of the assembly was assumed to be unaffected by d.o.i. and joint geometry. We therefore used a simpler joint model wherein the axes of the two cylindrical sections were assumed to intersect as shown in Figure 15. The joint region was assigned a Young's modulus, E_c, and the remainder of the model was given a Young's modulus of E. For all analyses, an aspect ratio of 100 is used.

Application of the Compliant Zone Model

Equating the expressions for Q and Q_c, we obtain an expression for K, per the definition for normalized K as

$$K_{\text{eq}} = \frac{KL}{EI}, \tag{13}$$

such that $K = f(l_c, L_1, L_2, E, E_c)$.

A graphical representation of the normalized K function is shown in Figure 16 for E_c/E ratios of 0.01, 0.5, and 0.1, respectively. Figure 16 illustrates that for any given ratio of E_c/E, and a sufficiently large compliant zone length, the assembly becomes a mechanism at larger values of L_1/L_2, resulting in negative K values. Thus, the validity of the model is dependent on the ratio of the moduli, and the length of the compliant zone in relation to the lengths of the beams in the assembly.

In Figure 17(a) and (b), plots of finite element results for E_{ffective}/E with $E_c/E = 0.01$ for the two values of l_c/L given in Figure 16(a) are shown. The value of K obtained for $L_1 = L_2$ ($KL/EI = 0.72$) is demonstrated to provide a good fit of the finite element data for $l_c/$

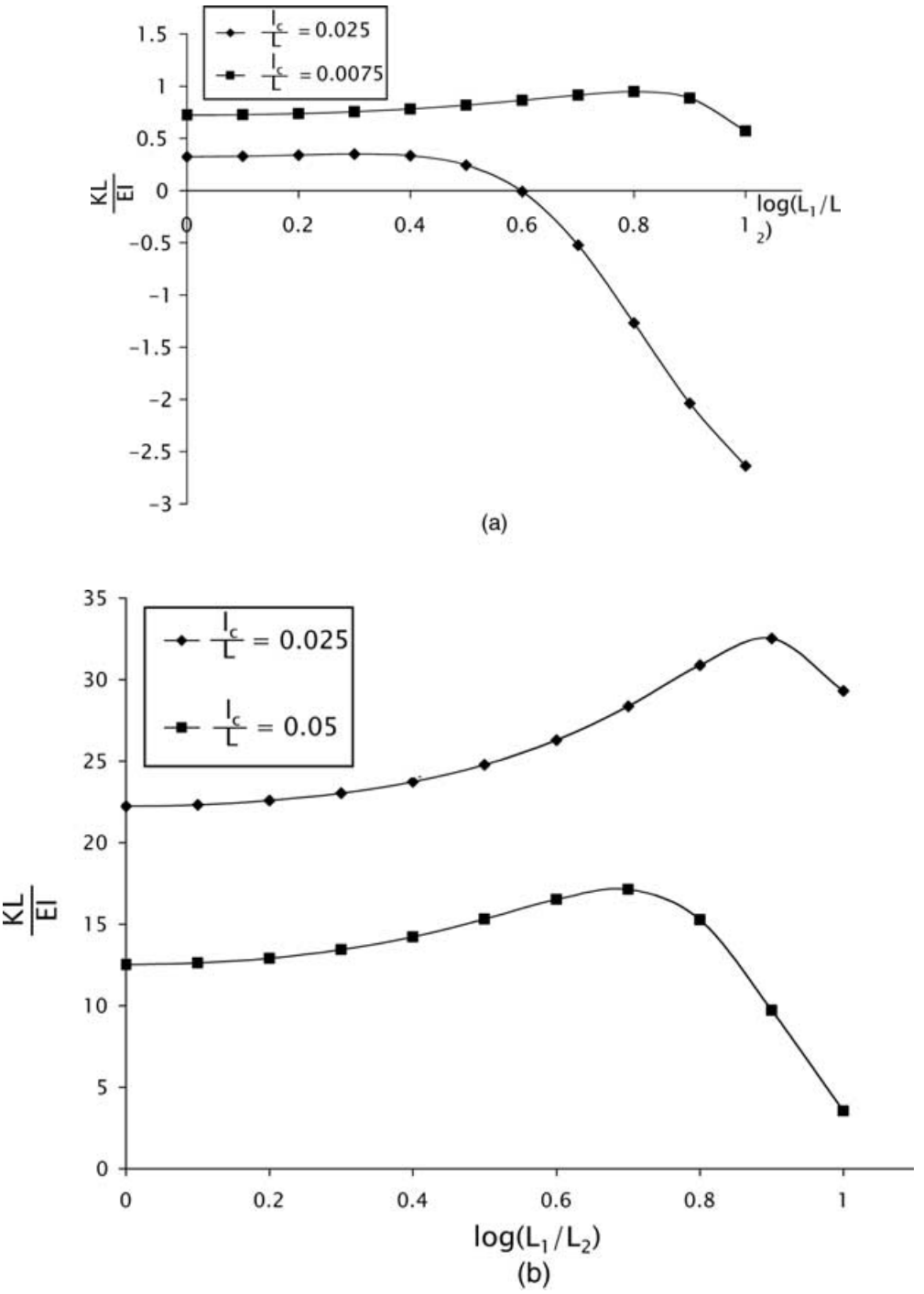

Figure 16. *Normalized torsion spring constant (KL/EI) versus log(L_1/L_2) results with (a) $E_c/E = 0.01$; (b) $E_c/E = 0.5$; and (c) $E_c/E = 0.1$.*

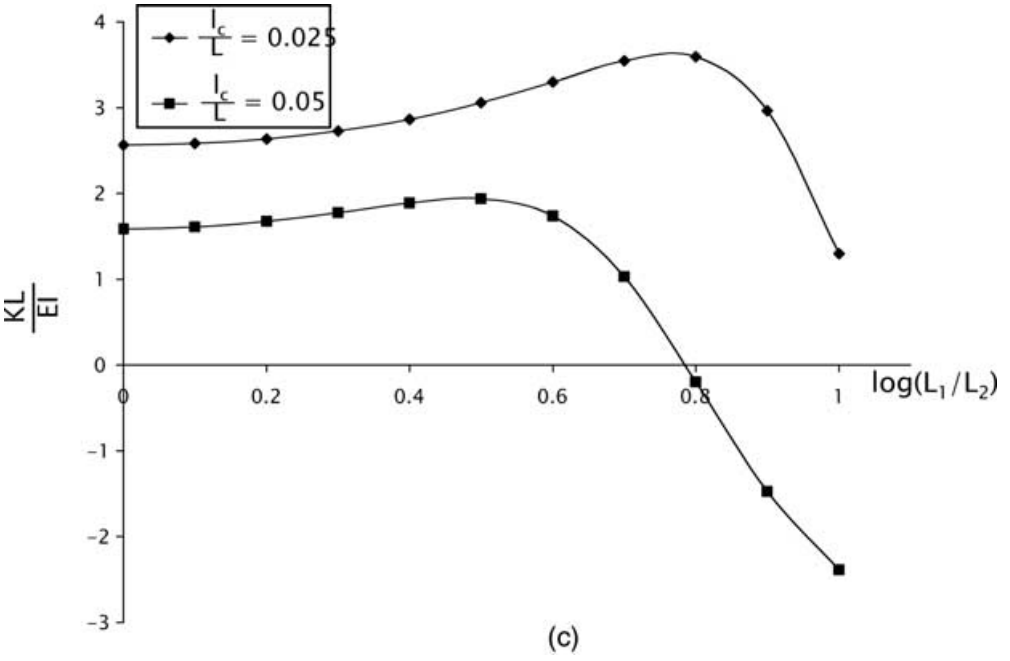

Figure 16. *Continued.*

$L = 0.0075$ over the full range of values of L_1/L_2 considered (Figure 17(a)). For the case of $L_1 = L_2$, the K_{eq} can be written as

$$K_{\text{eq}} = -\frac{\begin{array}{l}16\sin(\alpha)^2 A l_c^2\left[E_c^2(L-l_c)^2 + l_c^2E^2 + E_cE\left(2Ll_c - 2l_c^2 - L^2\right)\right] - L^4E_c^2A\sin(\alpha)^2 \\ +24I\cos(\alpha)^2\left[4l_c^2E(2E-3E_c) + L^2E_c^2 + 4E_cl_c(E_cl_c - E_cL + LE)\right]\end{array}}{l_c(E-E_c)\left[\sin(\alpha)^2 A\left[4l_c^3(E-E_c) + E_c\left(8Ll_c^2 - 5L^2l_c + L^3\right)\right] + 48Il_cE\cos(\alpha)^2\right]}. \tag{14}$$

Figure 17(b) shows that for the case of $l_c/L = 0.025$, the finite element results are well described by torsion spring model results with $KL/EI = 0.32$ (the value of K_{eq} from Equation (2) with $l_c/L = 0.025$, and $E_c/E = 0.01$) for $L_1/L_2 \leq 0.6$, but not for larger values. This result is consistent with the results presented in Figure 16(a), which show negative values for K for $L_1/L_2 > 0.6$.

Figure 17(a) and (b) also confirm that the finite element results for the effective modulus for single-phase beams ($l_c = 0$), are consistent with the 2D rigid bond ($K \to \infty$) results. This suggests that, even though stress singularities would necessarily arise in the joint region along the sharp line of intersection of the two cylindrical surfaces, the maximum forces and stresses away from the joint are unaffected by the joint geometry, and are consistent with the 2D solution.

Figure 18 are plots of effective modulus results versus $\log(L_1/L_2)$ with the more physically realistic E_c/E ratios of 0.1 and 0.5 for l_c/L values of 0.025 and 0.05 respectively. Figure 18(a) demonstrates the good correlation between the FEA results and the $E_{\text{effective}}$

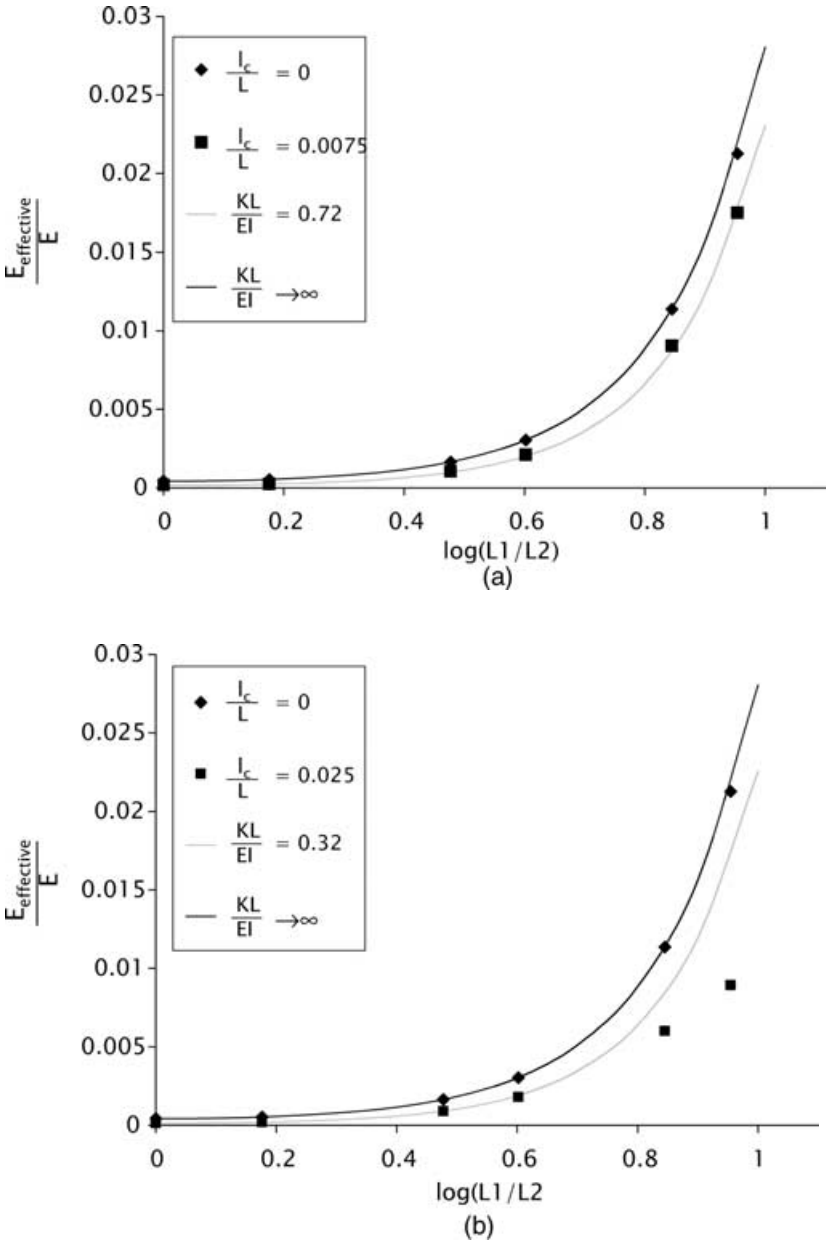

Figure 17. *Normalized effective modulus ($\gamma = 90°$) for torsion spring model with normalized spring constant KL/EI, and 3D compliant zone model with $E_c/E = 0.01$ for (a) $l_c/L = 0.0075$ and (b) $l_c/L = 0.025$.*

results with the torsion spring constant taken as the value obtained with $l_c/L = 0.025$ and $L_1 = L_2$ for each of the values of E_c/E plotted. In Figure 18(b), the FEA results for $l_c/L = 0.05$ and $E_c/E = 0.5$ are well fit with the results for K_{eq} with $L_1 = L_2$, $l_c/L = 0.05$, and $E_c/E = 0.5$), but the FEA results for $E_c/E = 0.1$ are only fit with the corresponding results for K_{eq} with $L_1 = L_2$, $l_c/L = 0.05$, and $E_c/E = 0.1$) for $L_1/L_2 < 0.75$. This is expected, since in this case, for $L_1/L_2 > 0.75$, K is negative (Figure 16(c)).

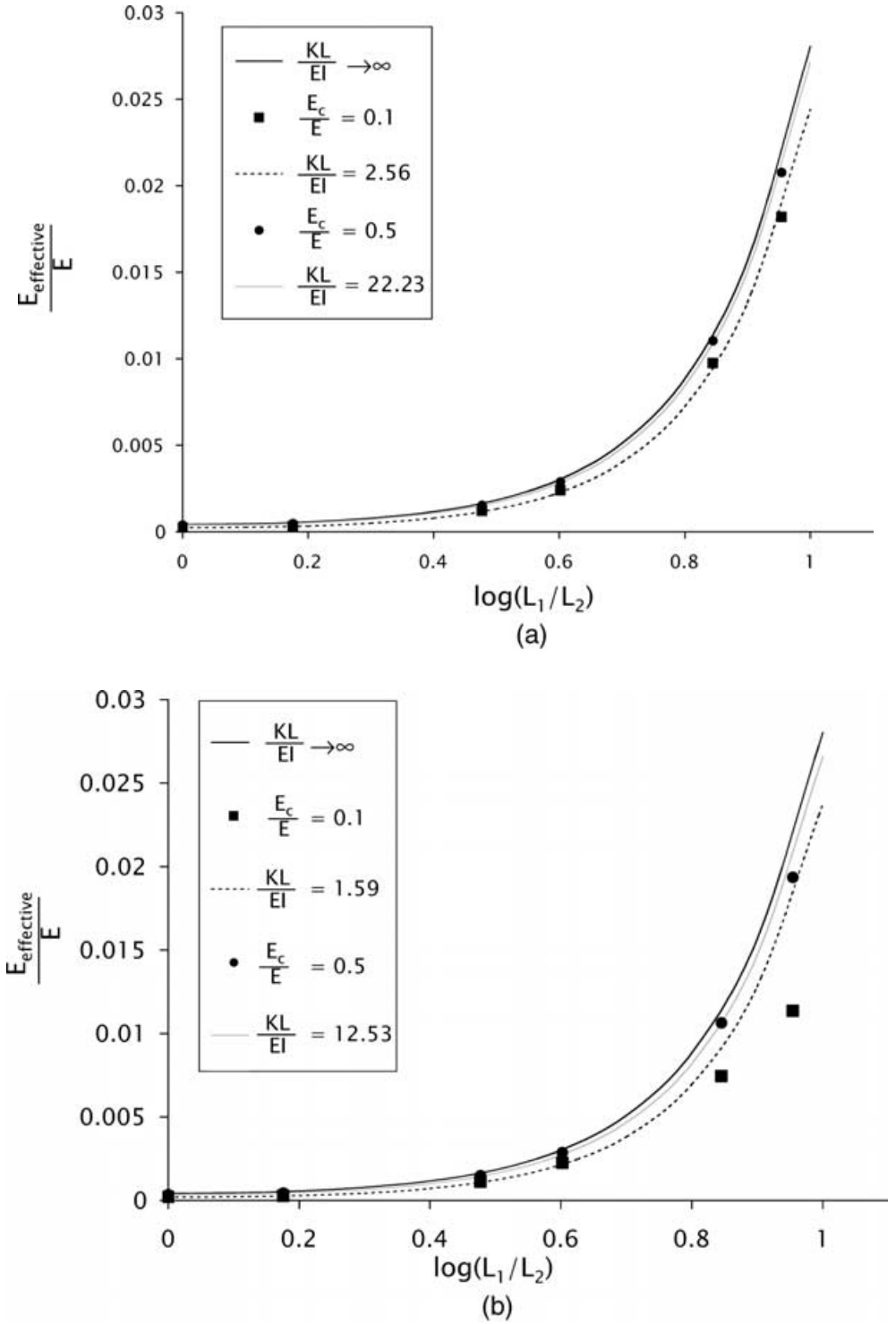

Figure 18. *Normalized effective modulus ($\gamma = 90^\circ$) for torsion spring model with normalized spring constant KL/EI, and 3D compliant zone model with $E_c/E = 0.1$ and $Ec/E = 0.5$ for (a) $l_c/L = 0.025$ and (b) $l_c/L = 0.05$.*

These analyses confirm the equivalence of the compliant zone model and the torsion spring model, and hence its usefulness in determining bulk properties such as effective modulus.

DISCUSSION

The performance of fused, porous networks is determined largely by the performance of the interfiber and interparticle bonds in the material. By modeling these joints and devising parameters for interpretation of equivalent two-beam simulations, we are able to study the effect of 'd.o.i.' on maximum stresses at the joint. The use of a two-beam assembly allows us to compare our finite element results with the solution of the simple equivalent 2D beam problem.

The models here reflect guidance from image analysis of actual materials, though our representations are undoubtedly idealized. However, modeling the joint in this way serves as a consistent means of creating models of different intersection angles and d.o.i., in order to provide some guidance in manufacturing porous materials. As the plots of Figure 13 show, Equation (7) appears to provide a reasonable approximation for the maximum joint stresses in such a 3D assembly, for any combination of intersection angle and d.o.i. As evidenced from calculated S' values, the shear stress component of the maximum joint stress (and thus the maximum total stress) is inversely related to d.o.i. For example, in Figure 13(c) for $\gamma = 90^\circ$, a decrease in d.o.i. from 0.85 to 0.52 leads to a 254% increase in maximum stress at the joint when $L_1/L_2 = 1$. For $\gamma \leq 90^\circ$, this effect was enhanced for smaller intersection angles. For example, for the case of d.o.i. $= 0.65$, the normalized shear factors for intersection angles of 45, 60, and 90° were found to be 2.72, 1.40, and 0.68, respectively. Note that for $\gamma = 120^\circ$ the corresponding value of S' is 1.06, showing that the inverse relationship of shear factor to intersection angle does not extend to obtuse angles. The largest deviations of stress values from the 2D solutions were observed at $\gamma = 45^\circ$ (the smallest angle in our analyses), with even 'large' values of degree of intersect having high shear factors. For example, for d.o.i. $= 0.85$, S' was found to be 2.22. When $L_1/L_2 = 7$, this translates to a maximum joint stress that is 2.75 times the maximum joint stress of the equivalent 2D assembly. Comparably, for $\gamma = 90^\circ$ and d.o.i. $= 0.85$, $S' = 0.62$ and for $L_1/L_2 = 7$, the maximum joint stress is only 30% higher than the 2D value.

We note that Equation (7) is independent of the lengths of the members of the assembly. Thus segment length determination through image analysis may not be required for fitting appropriate shear factors, though intersection angle and fillet radius are clearly required. The plots of Figure 13 also show that for small d.o.i., the shear factor increases significantly with even small decreases in d.o.i. For example, for $\gamma = 90^\circ$, the shear factor more than doubles with a decrease in d.o.i. from 0.55 to 0.52. Accuracy in correlating fillet radius with d.o.i is therefore of particular importance at these small d.o.i.

CONCLUSIONS/FUTURE WORK

Modification of joint properties in analysis of a 2D solution to capture complex 3D stresses appears promising, in both efficiency and accuracy of analysis. Each of the simple two-beam finite element analyses presented here required approximately an hour of

computational time. Fully 3D analysis of entire networks would thus be impractical, whereas an entire 2D network could probably be analyzed in seconds, using a modified joint property.

The joint models presented here, namely the volume-conserving joint and the compliant zone model, have been shown to capture the local and structural properties, respectively, of porous fibrous network elements. The results of our simulations with the volume-conserving fillet show that the maximum local stress at the intersection of two fibers is highly dependent on the d.o.i. of the joint, with small d.o.i. yielding high local stresses which can be several times that of an equivalent 2D model. A fully 3D real network material will necessarily contain many such joints, and therefore the potential for many regions of high local stresses. Based on our findings, one way of improving the structural performance of fused fibrous networks would be to increase the d.o.i. of the joints.

In this work we illustrated the volume-conserving model using one aspect ratio and one loading magnitude. Changing either of these factors will result in different shear factors. Before this model can be implemented as outlined in Figure 3, more 3D simulations involving different load conditions, aspect ratios, as well as intersection angles and d.o.i.s must be performed, with special attention paid to smaller d.o.i.

Future work will thus focus on examining the joints between a variety of network elements. By first developing a suitable geometric model for the joints and then investigating the stress concentrations and stress distributions at these interconnects, we hope to gain insight into the role of joint performance in a wider class of materials.

FUTURE APPLICATIONS

Nanotube sheets or papers, comprised of entangled nanotube bundles, are among the newest examples of fused porous networks. Junctions between nanotubes (e.g. [41]) have been studied in some detail. And advancements in manufacturing processes for connecting nanotubes, including soldering [42] and welding [43], are continually being reported. Indeed, nanotude junctions are key to the use of nanotubes in nanostructures and nanoscale electronic devices.

We are currently investigating the nature of the bonds nanotube sheets (specifically those comprised of nanotubes manufactured by the HiPCo process [44]), and the applicability of our earlier work in modeling stochastic networks, together with the results presented in this paper to this new material.

ACKNOWLEDGMENTS

The authors gratefully acknowledge support for this work from the DARPA Synthetic Multifunctional Materials Program (Dr. Leo Christodoulou, Program Manager, DARPA-DSO and Dr. Steve Fishman, Program Manager, ONR). Support from a PECASE from the National Science Foundation (Sastry) is also gratefully acknowledged.

LIST OF SYMBOLS

A = cross-sectional area of beam segments.
d = diameter of beam segments.

E = Young's Modulus of beam segments.
E_c = Young's Modulus of material in compliant zone.
E_{ffective} = effective modulus of two-beam assembly.
F_{AB} = axial force in segment AB.
F_{BC} = axial force in segment BC.
I = second moment of area of each beam.
K = torsion spring constant in torsion spring model.
K_{eq} = normalized torsion spring constant.
L_1 = length of segment AB of two-beam assembly.
L_2 = length of segment BC of two-beam assembly.
L_3 = horizontal distance AC of two-beam assembly.
$L = L_1 + L_2$.
l_c = length of compliant zone.
L_e = element length.
M = resultant moment at end C.
M_C = resultant moment at end C for the compliant zone model.
M_{AB} = bending moment in segment AB.
M_{BC} = bending moment in segment BC.
M_B = bending moment at B.
P = resultant force in y-direction at end C.
P_C = resultant force in y-direction at end C for the compliant zone model.
Q = resultant force in x-direction at end C.
Q_C = resultant force in x-direction at end C for the compliant zone model.
r = radius of fiber segments.
S = shear factor.
S' = normalized shear factor.
T = width of joint.
X = applied displacement in x-direction at end C.
Y = applied displacement in y-direction at end C.
α = angle beam AB makes with horizontal.
β = angle beam BC makes with horizontal.
γ = intersection angle between beam segments AB and BC.
Θ = applied bending moment at end C.
σ_{2D} = maximum stress at joint B as obtained from 2D beam theory.
σ_{3D} = maximum stress at joint B of 3D model.
ξ_1 = local coordinate along beam AB.
ξ_2 = local coordinate along beam BC.

REFERENCES

1. Sastry, A.M., Wang, C.-W. and Berhan, L. (2001). Deformation and Failure in Stochastic Fibrous Networks: Scale, Dimension and Application, *Key Engineering Materials*, Vol. 200, pp. 229–250, Trans Tech Publications, Switzerland.
2. Sastry, A.M., Cheng, X. and Wang, C.W. (1998). Mechanics of Stochastic Fibrous Networks, *Journal of Thermoplastic Composite Materials*, **11**(3): 288–296.
3. Cheng, X. and Sastry, A.M. (1999). On Transport in Stochastic, Heterogeneous Fibrous Domains, *Mechanics of Materials*, **31**: 765–786.

4. Cheng, X., Sastry, A.M. and Layton, B.E. (2001). Transport in Stochastic Fibrous Networks, *Journal of Engineering Materials and Technology*, **123**: 12–19.
5. Cheng, X., Wang, C., Sastry, A.M. and Choi, S.B. (1999). Investigation of Failure Processes in Porous Battery Substrates: Part II – Simulation Results and Comparisons, *Journal of Engineering Materials and Technology*, **121**: 514–523.
6. Wang, C.W., Berhan, L. and Sastry, A.M. (2000). Structure, Mechanics and Failure of Stochastic Fibrous Networks: Part I – Microscale Considerations, *Journal of Engineering Materials and Technology*, **122**: 450–459.
7. Wang, C., Cheng, X., Sastry, A.M. and Choi, S.B. (1999). Investigation of Failure Processes in Porous Battery Substrates: Part I – Experimental Findings, *Journal of Engineering Materials and Technology*, **121**: 503–513.
8. Wang, C.W. and Sastry, A.M. (2000). Structure, Mechanics and Failure of Stochastic Fibrous Networks: Part II – Network Simulations and Application, *Journal of Engineering Materials and Technology*, **122**: 460–468.
9. Lu, W., Carlsson, L.A. and Andersson, Y. (1995). Micro-Model of Paper Part 1: Bounds on Elastic Properties, *Tappi Journal*, **78**(12): 155–164.
10. Lu, W. and Carlsson, L.A. (1996). Micro-Model of Paper Part 2: Statistical Analysis of the Paper Structure, *Tappi Journal*, **79**(1): 203–210.
11. Lu, W., Carlsson, L.A. and de Ruvo, A. (1996). Micro-Model of Paper Part 3: Mosaic Model, *Tappi Journal*, **79**(2): 197–205.
12. Taya, M. and Ueda, N. (1987). Prediction of the In-Plane Electrical Conductivity of a Misoriented Short Fiber Composite: Fiber Percolation Model Versus Effective Medium Theory, *Journal of Engineering Materials and Technology*, **109**: 252–256.
13. Sastry, A.M., Choi, S.B. and Cheng, X. (1998). Damage in Composite NiMH Positive Electrodes, *Journal of Engineering Materials and Technology*, **120**: 280–283.
14. Wang, C.W., Cook, K.A. and Sastry, A.M. (2003). Conduction in Multiphase Particulate/Fibrous Networks: Simulations and Experiments on Li-ion Anodes, *Journal of the Electrochemical Society*, **150**(3): A385–A397.
15. Kuczynski, G.C. (1949). Self-diffusion in Sintering of Metallic Particles. *Transactions of the American Institute of Mining and Metallurgical Engineers*, **185**: 169–178.
16. German, R.M. (1996). Solid State Sintering Fundamentals, *Sintering Theory and Practice*, pp. 68–72, John Wiley and Sons, Inc. Publication, New York.
17. Siddiqui, F.M.A. and Beseler, J.W. (1989). Stress Concentration Factors in Angled Flexural Members of Rectangular Cross-Section, *Journal of Vibration, Acoustics, Stress, and Reliability in Design*, **111**: 490–491.
18. Skopinsky, V.N. (1993). Numerical Stress Analysis of Intersecting Cylindrical Shells, *Journal of Pressure Vessel Technology*, **115**: 275–282.
19. Pilkey, W.D. (1997). Shoulder Fillets, *Peterson's Stress Concentration Factors*, **2nd Edn.**, pp. 135–174, Wiley-Interscience Publication, New York.
20. Roark, R.J. (1965). Miscellaneous Tables, *Formulas for Stress and Strain*, pp. 382–422, McGraw-Hill Publication, New York.
21. Eringen, A.C. and Suhubi, E.S. (1965). Stress Distribution at Two Normally Intersecting Cylindrical Shells, *Nuclear Structural Engineering*, **2**: 235–270.
22. Bijlaard, P.P., Dohrmann, R.J. and Wang, I.C. (1967). Stresses in Junction of Nozzle to Cylindrical Pressure Vessel for Equal Diameter of Vessel and Nozzle, *Nuclear Engineering and Design*, **5**: 349–365.
23. Hansberry, J.W. and Jones, N. (1969). A Theoretical Study of Elastic Behavior of Two Normally Intersecting Cylindrical Shells, *Journal of Engineering for Industry*, **91**(3): 563–572.
24. Xue, M.D., Chen, W. and Hwang, K.C. (1994). Stresses at the Intersection of Two Cylindrical Shells, *Nuclear Engineering and Design*, **154**: 231–238.
25. Khan, A.S. and Hsiao, C. (1984). Strain Field in Straight Cylindrical Shells due to Applied Forces on the Attached Shell. Part I: No Hole In The Intersection Region, *Journal of Strain Analysis*, **19**(4): 269–274.

26. Ma, A. and Sharp, J.V. (1997). Fatigue Design of Cast Steel Nodes in Offshore Structures Based on Research Data, In: *Proceedings of the Institution of Civil Engineers-Water Maritime and Energy*, **124**(2): 112–126.
27. Bathe, K.-J. (1996). Formulation and Calculation of Isoparametric Finite Element Matrices, *Finite Element Procedures*, pp. 369–371, Prentice Hall Publication, Englewood Cliffs, New Jersey.
28. Cook, R.D., Malkus, D.S. and Plesha, M.E. (1989). Topics in Structural Mechanics, *Concepts and Applications of Finite Element Analysis*, pp. 248–250, John Wiley and Sons, Inc. Publication, New York.
29. Panagiotopoulos, G.D. (1984). A Finite Element Procedure for the Stress Analysis of Tubular Joint Connections, *International Journal for Numerical Methods in Engineering*, **23**: 317–329.
30. Wang, C.M., Reddy, J.N. and Lee, K.H. (2000). Bending of Beams, *Shear Deformable Beams and Plates: Relationships with Classical Solutions*, pp. 17–20, Elsevier Science Publication, Oxford.
31. Shigley, J.E. and Mischke, C.R. (1989). Deflection and Stiffness, *Mechanical Engineering Design*, p. 111, McGraw-Hill Publication, New York.
32. Timoshenko, S.P. and Gere, J.M. (1972). Shear Deflection in Beams, *Mechanics of Materials*, p. 372, Van Nostrand Reinhold Company Publication, New York.
33. Hutchinson, J.R. (2001). Shear Coefficients for Timoshenko Beam Theory, *Journal of Applied Mechanics*, **68**(1): 87–92.
34. Pai, P.F. and Schulz, M.J. (1999). Shear Correction Factors and An Energy-Consistent Beam Theory, *International Journal of Solids and Structures*, **36**(10): 1523–1540.
35. Ashby, M.F. (1987). Technology of the 1990s: Advanced Materials and Predictive Design, *Philosophical Transactions of the Royal Society of London A*, **322**(1567): 393–403.
36. Reddy, J.N. (1997). Classical and First Order Laminate Theories, *Mechanics of Laminated Composite Plates*, pp. 161–164, CRC Press Publication, Boca Raton.
37. Bert, C.W. (1973). Simplified Analysis of Static Shear Factors for Beams of Nonhomogeneous Cross Section, *Journal of Composite Materials*, **7**: 525–529.
38. Whitney, J.M. (1973). Shear Correction Factors for Orthotropic Laminates Under Static Load, *Journal of Applied Mechanics*, **40**: 302–304.
39. Ahn, S. (1998). High Capacity, High Rate Lithium-Ion Battery Electrodes Utilizing Fibrous Conductive Additives, *Electrochemical and Solid-State Letters*, **1**(3): 111–113.
40. Sypeck, D.J. and Wadley, H.N.G. (2001). Cellular Metal Truss Core Sandwich Structures, In: *Proceedings of the 2nd International Conference on Cellular Metals and Metal Foaming Technology* (MetFoam 2001), pp. 381–386, MIT-Verlag, Bremen.
41. Yao, Z., Postma, H.W.C., Balents, L. and Dekker, C. (1999). Carbon Nanotube Intramolecular Junctions, *Nature*, **402**, 273–276.
42. Banhart, F. (2001). The Formation of a Connection between Carbon Nanotubes in an Electron Beam, *Nano Letters*, **1**(6): 329–332.
43. Terrones, M., Banhart, F., Grobert, N., Charlier, J.-C., Terrones, H. and Ajayan, P.M. (2002). Molecular Junctions by Joining Single-Walled Carbon Nanotubes, *Physical Review Letters*, **89**(7): article number 075505.
44. Nikolaev, P., Bronikowski, M.J., Bradley, R.K., Rohmund, F., Colbert, D.T., Smith, K.A. and Smalley, R.E. (1999). Gas-Phase Catalytic Growth of Single-Walled Carbon Nanotubes from Carbon Monoxide, *Chemical Physics Letters*, **313**: 91–97.